THE JOURNAL OF BIOLOGICAL CHEMISTRY VOL. 291, NO. 26, pp. 13421–13430, June 24, 2016

Structure and Mechanism of Isopropylmalate Dehydrogenase from *Arabidopsis thaliana*

INSIGHTS ON LEUCINE AND ALIPHATIC GLUCOSINOLATE BIOSYNTHESIS[*] [◆]

Received for publication, April 4, 2016, and in revised form, April 25, 2016 Published, JBC Papers in Press, May 2, 2016, DOI 10.1074/jbc.M116.730358

Soon Goo Lee, Ronald Nwumeh[1]**, and Joseph M. Jez**[2]

From the Department of Biology, Washington University, St. Louis, Missouri 63130

Isopropylmalate dehydrogenase (IPMDH) and 3-(2′-methylthio)ethylmalate dehydrogenase catalyze the oxidative decarboxylation of different β-hydroxyacids in the leucine- and methionine-derived glucosinolate biosynthesis pathways, respectively, in plants. Evolution of the glucosinolate biosynthetic enzyme from IPMDH results from a single amino acid substitution that alters substrate specificity. Here, we present the x-ray crystal structures of *Arabidopsis thaliana* IPMDH2 (AtIPMDH2) in complex with either isopropylmalate and Mg^{2+} or NAD^+. These structures reveal conformational changes that occur upon ligand binding and provide insight on the active site of the enzyme. The x-ray structures and kinetic analysis of site-directed mutants are consistent with a chemical mechanism in which Lys-232 activates a water molecule for catalysis. Structural analysis of the AtIPMDH2 K232M mutant and isothermal titration calorimetry supports a key role of Lys-232 in the reaction mechanism. This study suggests that IPMDH-like enzymes in both leucine and glucosinolate biosynthesis pathways use a common mechanism and that members of the β-hydroxyacid reductive decarboxylase family employ different active site features for similar reactions.

The evolution of specialized metabolic pathways from primary metabolism provides plants with the ability to generate molecules that contribute to their survival (1). The classic cycle of gene duplication and divergence of sequence that leads to new substrate specificities is at the core of how plants diversify metabolism for new purposes. One example of this process is the evolution of enzymes from leucine biosynthesis into variants for the production of sulfur-containing glucosinolates in plants of the order Brassicales (2–4). In the biosynthesis of methionine-derived glucosinolates, the sequential addition of methylene groups that leads to elongated aliphatic glucosinolates mimics the reactions in leucine biosynthesis (2).

In the leucine biosynthesis pathway of plants and microbes, the NAD^+-dependent enzyme isopropylmalate dehydrogenase (IPMDH)[3] catalyzes the oxidation and decarboxylation of 3-isopropyl-L-malate (IPM) to 4-methyl-2-oxovalerate (Fig. 1) (2). Subsequent transamination of 4-methyl-2-oxovalerate produces leucine. In the synthesis of aliphatic glucosinolate biosynthesis, the corresponding 3-malate derivative (*i.e.* 3-(2′-methylthio)ethylmalate) is produced from methionine. Branched-chain aminotransferases catalyze the deamination of methionine to 4-methythio-2-oxobutanoic acid (5, 6). Subsequent steps performed by methylthioalkylmalate synthase and an isopropylmalate isomerase homolog generate 3-(2′-methylthio)ethylmalate) (7, 8), which undergoes oxidation and decarboxylation to yield 5-methylthiol-2-oxopentoate (Fig. 1) (9, 10). This product can then be transaminated for further elongation of the aliphatic moiety to yield C4 to C8 aliphatic glucosinolates (2).

In plants, complementation of yeast with a *Leu2* mutation by genes from canola, potato, and *Arabidopsis thaliana* identified IPMDH in the leucine biosynthesis pathway (11–13). Later studies of the three IPMDH isoforms in Arabidopsis (AtIPMDH1–3) revealed differences in the biochemical properties and metabolic contributions of each protein (9, 10). Steady-state kinetic analysis of AtIPMDH1–3 showed that each enzyme catalyzed the conversion of 3-isopropylmalate to 4-methyl-2-oxovalerate; however, the catalytic efficiency of AtIPMDH1 was up to 40-fold lower than the two other isoforms (9, 10). Analysis of Arabidopsis T-DNA insertion mutants that disrupted *AtIPMDH1* showed decreased levels of C4–C8 aliphatic glucosinolates and leucine. The loss of glucosinolate synthesis could be complemented by expression of AtIPMDH1 but not by expression of either AtIPMDH2 or AtIPMDH3 (10). T-DNA mutants of *AtIPMDH2* and *AtIPMDH3* reduced leucine levels but did not significantly alter glucosinolate production in Arabidopsis (14). Moreover, the Arabidopsis *AtIPMDH2*/*AtIPMDH3* double mutant had defects in pollen and embryo sac development, which were consistent with a role for leucine synthesis in gametophyte formation (14). These results indicate that AtIPMDH1 functions primarily in the oxidative decarboxylation step of the aliphatic glucosinolate biosynthesis and that AtIPMDH2 and AtIPMDH3 are dedicated to leucine biosynthesis (11–14).

[*] This work was supported in part by National Science Foundation Grant MCB-0904215. Portions of this research were carried out at the Argonne National Laboratory Structural Biology Center of the Advanced Photon Source, a national user facility operated by the University of Chicago for the Department of Energy Office of Biological and Environmental Research Grant DE-AC02–06CH11357. The authors declare that they have no conflicts of interest with the contents of this article.

[◆] This article was selected as a Paper of the Week.

The atomic coordinates and structure factors (codes 5J32, 5J33, and 5J34) have been deposited in the Protein Data Bank (http://wwpdb.org/).

[1] Supported in part by the Washington University Summer Scholars Program in Biology and Biomedicine and the Washington University uSTAR Summer Scholars Program.

[2] To whom correspondence should be addressed. E-mail: jjez@wustl.edu.

[3] The abbreviations used are: IPMDH, isopropylmalate dehydrogenase; IPM, 3-isopropyl-L-malate; ITC, isothermal titration calorimetry; PDB, Protein Data Bank; r.m.s.d., root mean square deviation.

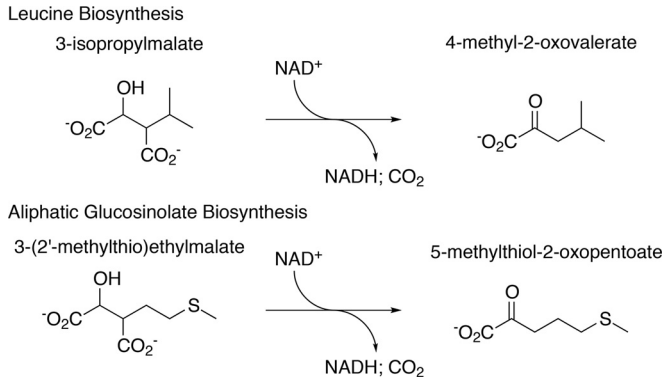

FIGURE 1. **Overall reactions catalyzed by 3-isopropylmalate dehydrogenase in leucine biosynthesis and 3-(2′-methylthio)ethylmalate dehydrogenase in aliphatic glucosinolate biosynthesis.**

Structural and functional studies revealed the point mutation responsible for functional divergence of the IPMDH for either leucine or aliphatic glucosinolate synthesis pathways in Arabidopsis (9). Substitution of an active site leucine in AtIPMDH2 and AtIPMDH3 for a phenylalanine in AtIPMDH1 altered substrate preference from IPM (AtIPMDH2 and AtIPMDH3) to 3-(2′-methylthio)ethylmalate (AtIPMDH1) (9). In addition, complementation of the Arabidopsis *AtIPMDH1* T-DNA knock-out with genes encoding either AtIPMDH2 or AtIPMDH3 with the phenylalanine substitution restored aliphatic glucosinolate production in transgenic plants (9). Although these studies reveal the evolutionary change required for substrate preference of IPMDH in leucine and aliphatic glucosinolate synthesis, the common reaction chemistry of these enzymes remains unexplored.

Here, we present the x-ray crystal structures of AtIPMDH2 in complex with either IPM or NAD^+. These structures provide details on substrate and NAD(H) recognition, show conformational shifts upon ligand binding, and suggest a model for catalysis. Site-directed mutagenesis of active site residues support the role of a catalytic lysine and Mg^{2+} ion during the oxidation and decarboxylation reactions performed by AtIPMDH2. In addition, the x-ray crystal structure of the AtIPMDH2 K232M mutant shows that mutation of the catalytic residue does not significantly alter the overall architecture of the active site and retains substrate binding. These studies reveal the molecular basis for the conserved reaction chemistry of plant IPMDH isoforms in both leucine- and methionine-derived glucosinolate biosynthesis.

Experimental Procedures

Materials—Generation of the pET-28a-AtIPMDH2 bacterial expression construct was as described previously (9). The expression construct removes the chloroplast localization tag of AtIPMDH2 (9). All oligonucleotides for generating AtIPMDH2 site-directed mutants were from IDT. All reagents were purchased from Sigma, unless otherwise noted.

Protein Expression and Purification—Escherichia coli BL21 (DE3) cells were transformed with the pET-28a-AtIPMDH2 vector and grown in Terrific broth containing 50 μg ml^{-1} kanamycin at 37 °C (250 rpm) until $A_{600\,nm}$ = 0.6–0.8. Addition of isopropyl 1-thio-β-D-galactopyranoside (1 mM final) induced protein expression. Cells were then grown overnight (18 °C). Cell pellets were harvested by centrifugation (10,000 × *g*; 10 min) and resuspended in lysis buffer (50 mM Tris, pH 8.0, 500 mM NaCl, 20 mM imidazole, 1 mM β-mercaptoethanol, 10% (v/v) glycerol, and 1% (v/v) Tween 20). Following lysis by sonication, cell debris was removed by centrifugation (30,000 × *g*; 45 min) and the supernatant passed over a Ni^{2+}-nitriloacetic acid (Qiagen) column equilibrated with wash buffer (lysis buffer minus Tween 20). After loading, the column was washed with 10 column volumes of wash buffer. Bound fusion protein was eluted with elution buffer (wash buffer with 250 mM imidazole) and collected. For removal of the His tag, thrombin (1/1000th of total protein) was added to the sample and dialyzed overnight (4 °C) *versus* 25 mM HEPES, pH 7.5, 100 mM NaCl, and 5 mM $MgCl_2$. After dialysis, passage of the sample over a mixed Ni^{2+}-nitriloacetic acid/benzamidine-Sepharose column removed thrombin and uncleaved His-tagged protein. Size-exclusion chromatography of the flow-through was performed on a Superdex-200 26/60 HiLoad FPLC column equilibrated with dialysis buffer. Peak fractions were collected and concentrated using centrifugal concentrators (Amicon) with protein concentration determined using the Bradford assay with bovine serum albumin as the standard. Purified protein was flash-frozen in liquid nitrogen and stored at −80 °C.

Site-directed Mutagenesis—The L132A, L133A, R136A, R136K, R146K, R146A, R174A, R174K, Y181A, Y181F, Y181H, K232M, N234A, N234D, V235A, D264N, D288N, and D292N point mutants of AtIPMDH2 were generated using the QuikChange PCR method (Agilent) with pET-28a-AtIPMDH2 as template and confirmed by sequencing (Washington University DNA Sequencing Facility). Protein expression and purification of the mutants were performed as described above using Ni^{2+}-affinity and size-exclusion chromatographies.

Protein Crystallography—Crystals of AtIPMDH2 grew at 4 °C in hanging drops (2 μl) from a 1:1 ratio of protein (10 mg ml^{-1}). The AtIPMDH2·NAD^+ complex was obtained from crystals grown in 1.25 M ammonium sulfate, 0.1 M HEPES, pH 7.5, and 5 mM NAD^+. Crystals of the AtIPMDH2·IPM·Mg^{2+} complex grew in 1.0 M ammonium phosphate, 0.1 M imidazole, pH 8.0, and 5 mM IPM. The AtIPMDH2 K232M crystals were from 0.16 M ammonium sulfate, 0.07 M sodium acetate, 17.5% (v/v) PEG-4000, and 20% (v/v) glycerol. For data collection, crystals of wild-type protein were soaked in mother liquor supplemented with 25% glycerol, as cryoprotectant. The K232M mutant crystals were directly flash-frozen in liquid nitrogen. X-ray diffraction data (0.5° oscillations; 360 images; 100 K) were collected at Structural Biology Center beamline 19-ID of the Argonne National Laboratory Advanced Photon Source. Integration, merging, and scaling of diffraction data used HKL3000 (15). The structure of AtIPMDH2 in complex with IPM was solved by molecular replacement using the apoenzyme structure of AtIPMDH2 (PDB code 3R8W (9)) using PHASER (16). Four molecules in the asymmetric unit were found in the molecular replacement solution. The three-dimensional model was build using COOT (17) and refined in PHENIX (Table 1) (18). The structures of the AtIPMDH2·NAD^+ complex and the AtIPMDH2 K232M mutant were solved by molecular replacement using the AtIPMDH2·IPM·Mg^{2+} complex structure with

TABLE 1
Crystallographic data collection and refinement statistics

	AtIPMDH2·IPM·Mg^{2+}	AtIPMDH2·NAD^+	AtIPMDH2-K232M
Crystal			
Space group	$P2_1$	$P2_12_12_1$	$P2_1$
Cell dimensions	a = 96.06 Å, b = 49.62 Å, c = 158.9 Å; β = 105.4°	a = 77.20 Å, b = 132.9 Å, c = 349.4 Å	a = 76.80 Å, b = 76.82 Å, c = 209.5 Å; β = 90.2°
Data collection			
Wavelength (Å)	0.979	0.979	0.979
Resolution range (Å) (highest shell)	32.5–1.93 (1.96–1.93)	46.7–3.49 (3.55–3.49)	38.4–1.83 (1.86–1.83)
Reflections (total/unique)	330,270/104,824	305,383/45,923	701,003/211,778
Completeness (highest shell)	96.4% (92.6%)	98.6% (97.0%)	98.8% (99.4%)
$\langle I/\sigma \rangle$ (highest shell)	11.0 (2.0)	6.4 (2.0)	28.6 (2.0)
R_{sym} [a] (highest shell)	9.3% (62.4%)	24.4% (58.6%)	8.9% (41.9%)
Refinement			
R_{cryst} [b]/R_{free} [c]	15.9%/19.8%	18.9%/25.7%	16.5%/18.5%
No. of protein atoms	11,003	21,702	11,012
No. of waters	1,434		1,517
No. of ligand atoms	52	337	35
r.m.s.d. bond lengths (Å)	0.007	0.013	0.006
r.m.s.d. bond angles (°)	1.021	1.364	1.011
Average B-factor (Å^2)-protein, water, ligand	19.3, 34.0, 23.4	78.1, 66.7, –	36.4,49.4, 58.7
Stereochemistry: most favored, allowed, outliers	97.2, 2.8, 0%	95.6, 4.4, 0%	97.1, 2.9, 0%

[a] $R_{sym} = \Sigma|I_h - \langle I_h \rangle|/\Sigma I_h$, where $\langle I_h \rangle$ is the average intensity over symmetry.
[b] $R_{cryst} = \Sigma|F_o - \langle F_c \rangle|/\Sigma F_o$, where summation is over the data used for refinement.
[c] R_{free} is defined the same as R_{cryst}, but it was calculated using 5% of data excluded from refinement.

ligand coordinates removed as a search model. Model building and refinement were as described above (Table 1). Coordinates and structure factors for the AtIPMDH2·IPM·Mg^{2+} (PDB code 5J32), AtIPMDH2·NAD^+ (PDB code 5J33), and AtIPMDH2 K232M mutant ((PDB code 5J34) were deposited in the Protein Data Bank.

Enzyme Assays—Steady-state kinetic assays were performed at 25 °C in a standard assay mix of 0.1 M Tris, pH 7.5, 1 mM $MgCl_2$, 100 mM KCl, and 5 mM NAD^+ with varied IPM concentrations (0–0.1 mM) (9, 10). All assays were performed in a 96-well plate format (100 μl volume) using a Tecan UV-visible plate reader. For mutant assays, IPM concentrations up to 10 mM were used. Protein amounts ranging from 0.1 μg (wild-type AtIPMDH2) to 100 μg (less active AtIPMDH2 mutants) were used. The resulting initial velocity data were fit to the Michaelis-Menten equation, $v = V_{max}\cdot[S]/(K_m + [S])$, using SigmaPlot.

Isothermal Titration Calorimetry—ITC experiments were performed at 15 °C using a VP-ITC calorimeter (Microcal, Inc.). Wild-type and K232M mutant proteins were dialyzed against 25 mM HEPES, pH 7.5, and 100 mM NaCl. Final protein concentrations were between 0.06 and 0.075 mM, and ligand concentrations were between 0.85 and 0.92 mM. For the titration against IPM, both protein and IPM were pre-incubated with 2 mM $MgCl_2$. Likewise, for the titration against NADH, both protein and NADH were pre-incubated with 2 mM IPM and 2 mM $MgCl_2$. The obtained data were fitted to single-site binding model, $Q_i^{tot} = V_0\cdot M_i^{tot}\cdot((nK_1x)\Delta H_1)/(1 + K_1x)$, using a modified version of Origin software (OriginLab) provided by the instrument manufacturer (Microcal, Inc.). Values for the change in Gibbs free energy (ΔG) were calculated using $\Delta G = -RT\ln(K_{eq})$, where r = 1.9872 cal K^{-1} mol^{-1}, and T is the temperature in Kelvin. Entropy changes (ΔS) were calculated using $\Delta G = \Delta H - T\Delta S$. K_d was calculated as $1/K_{eq}$.

Results

Overall Structure of AtIPMDH2—To determine the molecular basis of substrate and cofactor recognition by AtIPMDH2, the x-ray crystal structures of the IPM and NAD^+ complexes were determined at 1.93 and 3.49 Å resolution, respectively (Table 1). The overall structure of AtIPMDH2 is formed from two monomers related by non-crystallographic symmetry (Fig. 2). Each monomer contains a core anti-parallel β-sheet (β1a-b-i-h-c-d-g-e-f) with a set of α-helices (α1–4 and α9–11) on the exterior side of the β-sheet and another group of helices (α5–8) centered on the other half of the β-sheet along the dimer interface. An additional protruding β-sheet (β2a-b) extends the dimer interface. Compared with the previously reported apoenzyme structure (9), the three-dimensional structures of the IPM (1.1 Å root mean square deviation (r.m.s.d.) for 358 C_α atoms) and NAD^+ (1.6 Å r.m.s.d. for 360 C_α atoms) are similar. AtIPMDH2 shares a common three-dimensional fold and 40–60% amino acid sequence identity with homologs from multiple microorganisms, such as *E. coli*, *Salmonella typhimurium,* and *Thermus thermophilus* (19–21), with r.m.s.d. of 1.3–3.3 Å^2 for 340–360 C_α atoms (Z scores = 57.6–43.8). The DALI search also revealed three-dimensional fold conservation with other acid dehydrogenases, notably homoisocitrate dehydrogenase (Z scores = 45.6–41.2; C_α atom r.m.s.d. = 1.7–2.4; sequence identity = 35–40%) and isocitrate dehydrogenase (Z scores = 43.8–1.16; C_α atom r.m.s.d. = 1.9–3.8; sequence identity = 14–29%) (22–24). The structures of AtIPMDH2 in complex with either IPM or NAD^+ provide details on the binding of cofactor and substrate to the enzyme.

AtIPMDH2 NAD(H)-binding Site—A 20-Å-long cleft generally defined by α8 from one monomer and α7 from the adjacent monomer along the dimer interface and α4 on the opposite side is the location of NAD^+ binding in the AtIPMDH2 x-ray crystal structure (Figs. 2 and 3*A*). Clear electron density for NAD^+ allowed modeling of the ligand in the structure (Fig. 3*B*). Multiple interactions lock the nicotinamide cofactor in the binding site (Fig. 3*B*). A pocket formed by residues on β1i-α9 loop (residues 321–334) provides van der Waals contacts between the adenine ring of NAD^+ and His-321, Asn-334, and Asp-375. The

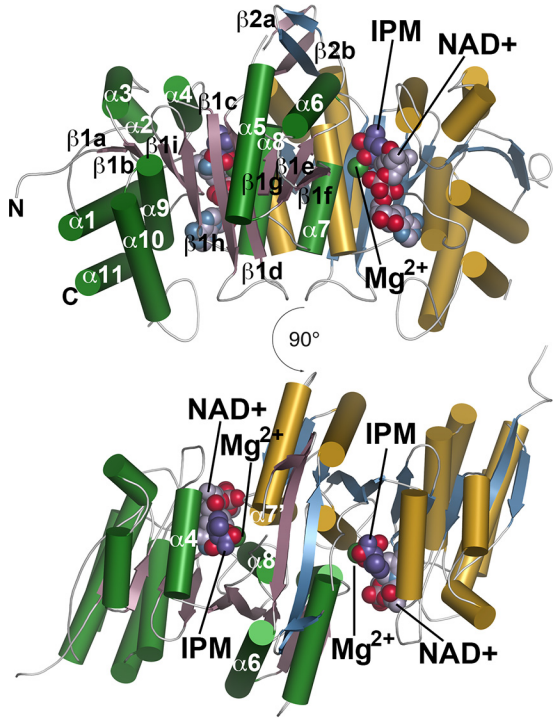

FIGURE 2. **Overall structure of AtIPMDH2.** Ribbon diagram shows the structure of the AtIPMDH2 dimer. One monomer is shown with labeled *green* α-helices and *rose* β-strands and the other monomer with *gold* α-helices and *blue* β-strands. The N- and C-terminal positions are indicated in the *left* monomer. Bound ligands are shown as space-filling models. The positions of IPM and Mg^{2+} are from the structure of AtIPMDH2·IPM·Mg^{2+}, and the position of NAD^+ is from the AtIPMDH2·NAD^+ structure. The bottom view is rotated 90° to highlight the location of the active site in each monomer. Key α-helices that surround the NAD(H)-binding site are labeled.

backbone nitrogen and carbonyl of Asn-334 formed hydrogen bonds with the N1 and the amine side chain of the adenine ring, respectively. Asp-326 forms a bidentate interaction with the hydroxyl groups of the adenine ribose. Residues of the β1i-α9 loop also interact with one of the phosphate groups of the bound cofactor with specific hydrogen bonds contributed by the backbone nitrogens of Gly-322 and Ala-324. The side-chain hydroxyl group of Ser-323 hydrogen bonds with the nicotinamide ribose ring oxygen. Glu-129 contributes a hydrogen bond to one of the hydroxyl groups of the nicotinamide ribose. The amide group of the nicotinamide is positioned by interactions with Ile-114 and Glu-318. Tyr-262, Asp-264, and Asn-265 from α7 of the adjacent monomer provide additional van der Waals contacts with the bound cofactor. Amino acid sequence comparison of residues in the NAD(H)-binding site of AtIPMDH2 with the other Arabidopsis isoforms and the IPMDH from *E. coli*, *T. thermophilus*, and *Saccharomyces cerevisiae* and the *T. thermophilus* homoisocitrate dehydrogenase and *S. cerevisiae* isocitrate dehydrogenase reveal the highly conserved sequence of the NAD(H)-binding site of these structurally related enzymes (Fig. 3*C*). As described below, the reactive nicotinamide ring is oriented toward the site of IPM binding in AtIPMDH2.

Comparison of apoenzyme and NAD^+-bound forms of AtIPMDH2 reveals structural changes that occur following cofactor binding (Fig. 3*D*). In both structures of AtIPMDH2, the surface cleft that forms the NAD(H)-binding site is solvent-accessible; however, the ligand-bound structure reveals a shift of the region, including α1–4 and α9–11, toward the dimer interface by 5–10 Å. This conformational change brings key residues, including Ile-114 and Glu-129 that interact with the amide group of the nicotinamide ring and residues of the β1i-α9 loop, into proximity of the cofactor and suggests that ligand binding may induce a conformational change.

AtIPMDH2 Active Site and IPM Binding—The AtIPMDH2·IPM·Mg^{2+} complex provides a detailed view of the active site and substrate interactions. As with the NAD(H)-binding site, the active site consists of residues contributed from α4 and α8 of one monomer and α7 of the adjacent monomer (Figs. 2 and 4). Unambiguous electron density for both IPM and Mg^{2+} was observed in the structure (Fig. 4*A*). Binding of the Mg^{2+} ion involves Asp-288 and Asp-292 from one monomer and Asp-264 from the adjacent monomer. In addition, the IPM α-carboxylate and β-hydroxyl groups also coordinate the Mg^{2+} ion. Multiple electrostatic interactions anchor IPM in the active site (Fig. 4*A*). The side-chain guanidinium groups of Arg-146 and Arg-136 interact with the α-carboxylate of the substrate. Similarly, the side chains of Lys-232 from the adjacent monomer and Arg-136 and Arg-174 form charge-charge interactions with the γ-carboxylate of IPM. The β-hydroxyl of the substrate hydrogen bonds with Asp-264. These interactions position the γ-isopropyl group of IPM toward Leu-132 and Leu-133. Substitution of Leu-133 for a phenylalanine in AtIPMDH1 alters substrate preference toward aliphatic glucosinolate substrates (9). Amino acid sequence comparisons of the IPMDH from Arabidopsis, *E. coli*, *T. thermophilus*, and *S. cerevisiae* show that with the exception of Leu-133, which is a phenylalanine in AtIPMDH1 from glucosinolate biosynthesis (9), all other positions in the active site are invariant. Binding of IPM in the AtIPMDH2 active site orients the substrate in proximity to the NAD(H)-binding site (Fig. 4*B*).

An overlay of the AtIPMDH2·NAD^+ and AtIPMDH2·IPM·Mg^{2+} structures provides a model for the initial Michaelis complex of the enzyme (Fig. 5). The β-alcohol of IPM is 2.3 Å away from the Mg^{2+} ion and 3.2 Å away from an active site water molecule, which in turn hydrogen bonds with Lys-232, Asn-234, and Asp-264, and 3.4 Å from the N_ζ of Lys-232. The C_4-position of the NAD^+ nicotinamide ring, which undergoes hydride transfer, is 3.0 Å distant from the C_2 of IPM. The positions of the substrates and residues in the AtIPMDH2 active site would allow for the oxidation and decarboxylation reactions that convert IPM to 4-methyl-2-oxovalerate in leucine biosynthesis. Moreover, the sequence conservation of active site residues with AtIPMDH1, which functions as a 3-(2′-methylthio)ethylmalate dehydrogenase in glucosinolate biosynthesis, suggests a common chemical mechanism between these related enzymes.

Site-directed Mutagenesis of AtIPMDH2 and Steady-state Kinetic Analysis—To examine the contribution of active site residues to catalysis (Figs. 4*A* and 5), the AtIPMDH2 L132A, L133A, R136K, R136A, R146A, R146K, R174A, R174K, Y181A, Y181F, Y181H, K232M, N234A, N234D, V235A, D264N, D288N, and D292N point mutants were generated by QuikChange PCR. Each mutant protein was expressed in *E. coli* and purified by nickel-affinity and size-exclusion chromatographies

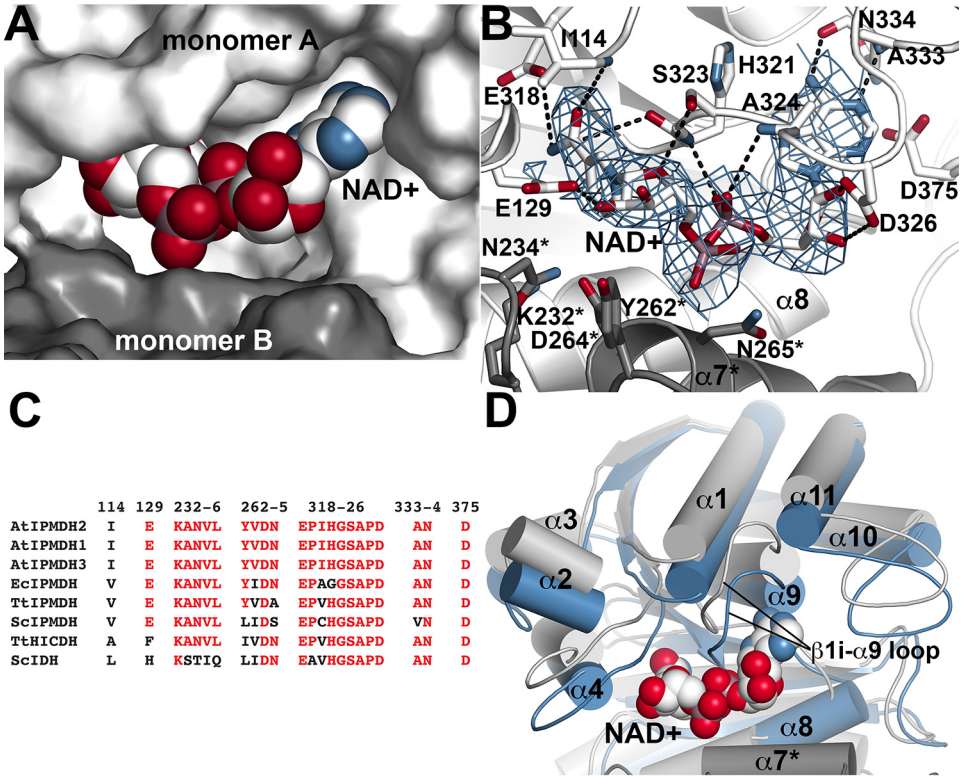

	114	129	232–6	262–5	318–26	333–4	375
AtIPMDH2	I	E	KANVL	YVDN	EPIHGSAPD	AN	D
AtIPMDH1	I	E	KANVL	YVDN	EPIHGSAPD	AN	D
AtIPMDH3	I	E	KANVL	YVDN	EPIHGSAPD	AN	D
EcIPMDH	V	E	KANVL	YIDN	EPAGGSAPD	AN	D
TtIPMDH	V	E	KANVL	YVDA	EPVHGSAPD	AN	D
ScIPMDH	V	E	KANVL	LIDS	EPCHGSAPD	VN	D
TtHICDH	A	F	KANVL	IVDN	EPVHGSAPD	AN	D
ScIDH	L	H	KSTIQ	LIDN	EAVHGSAPD	AN	D

FIGURE 3. **AtIPMDH2 NAD(H)-binding site.** *A,* surface rendering of the NAD(H) binding cleft. NAD^+ is shown as a space-filling model with surfaces corresponding to monomer A (*white*) and monomer B (*gray*) shown. *B,* protein-ligand interactions in the NAD(H)-binding site. The $2F_o - F_c$ omit map (1.5 σ) for NAD^+ is shown. The ligand and residues of the binding site are drawn as stick renderings with *dotted lines* indicating hydrogen bond interactions. Monomers A and B are differentially colored as in *A*. Residues from monomer B are indicated by an *asterisk*. *C,* amino acid sequence comparison of NAD(H)-binding site residues in IPMDH, homoisocitrate dehydrogenase, and isocitrate dehydrogenase. Conserved residues are indicated in *red*. A multiple sequence alignment of AtIPMDH2 (GI_AEE36420.1), AtIPMDH1 (NP_196924.1), AtIPMDH3 (SP_Q9FMT1.1), *T. thermophilus* TtIPMDH (GI_1942481), *E. coli* EcIPMDH (GI_5542195), yeast ScIPMDH (SP_P04173), *T. thermophilus* homoisocitrate dehydrogenase TtHICDH (DBJ_BAB88861.1), and yeast isocitrate dehydrogenase ScICDH (GI_167013439) was generated using the Multalign server. *D,* ligand-induced conformational changes in AtIPMDH2. The structures of the AtIPMDH2 apoenzyme (*gray*) and AtIPMDH2·NAD^+ complex (*blue*) are shown. NAD^+ is shown as a space-filling model.

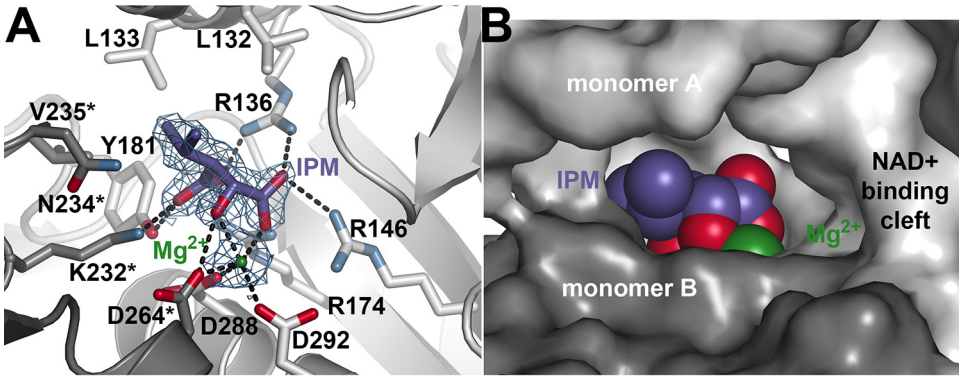

FIGURE 4. **AtIPMDH2 active site and IPM and Mg^{2+} binding.** *A,* IPM and Mg^{2+} binding in the active site. The $2F_o - F_c$ omit map (1.5 σ) for IPM (*purple*) and Mg^{2+} (*green*) is shown. The ligands and residues of the active site are drawn as stick renderings with *dotted lines* indicating electrostatic and hydrogen bond interactions. Monomers A and B are colored *white* and *gray*, respectively. Residues from monomer B are indicated by an *asterisk*. *B,* surface view of the active site. IPM and Mg^{2+} are shown as space-filling models with surfaces corresponding to monomer A (*white*) and monomer B (*gray*) shown. The location of the NAD(H) binding cleft is also indicated.

as a dimeric form, as observed for the wild-type enzyme. Initial assays using up to 100 μg of protein (200-fold more protein than in wild-type assays) indicated that the R136A, R174A, K232M, N234A, N234D, V235A, D264N, and D288N mutants displayed no significant activity above background; however, the other mutants were sufficiently active to determine steady-state kinetic parameters using IPM as a substrate (Table 2).

Within the AtIPMDH2 active site, mutation of residues near the γ-isopropyl group of IPM (*i.e.* Leu-132, Leu-133, and Val-235) resulted in 10–70-fold reductions in catalytic efficiency (k_{cat}/K_m) compared with the wild-type enzyme (Table 2). These effects largely resulted from increased K_m values. The V235A mutant displayed less than 2–3-fold changes in each steady-state kinetic parameter, whereas the L132A and L133A mutations showed greater differences.

The cluster of arginines (Arg-136, Arg-146, and Arg-174) is positioned to interact with the carboxylate groups of IPM (Fig. 4*A*). Although alanine substitutions of Arg-136 and

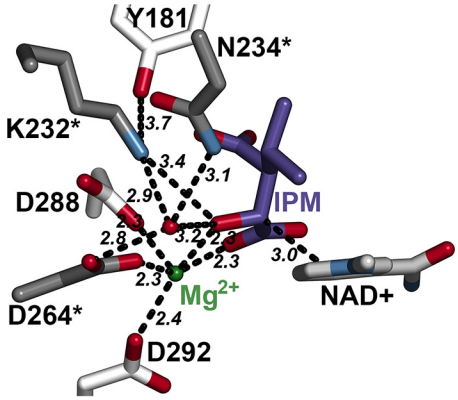

FIGURE 5. **Composite view of the AtIPMDH2 active site showing a putative substrate·cofactor complex.** The structures of the AtIPMDH2·NAD^+ and AtIPMDH2·IPM·Mg^{2+} complexes were overlaid. Amino acid side-chain positions are from the AtIPMDH2·IPM·Mg^{2+} complex. Ligands are from their respective structures. Residues from the adjacent monomer are indicated by an *asterisk*. *Dotted lines* denote key distances in the active site.

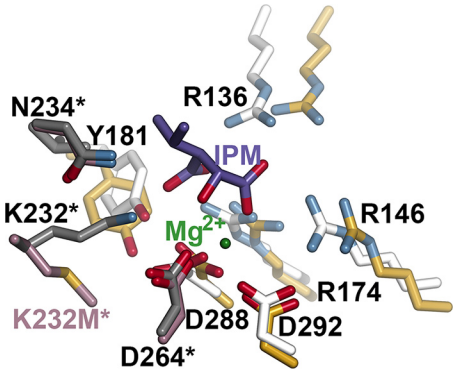

FIGURE 6. **Active site comparison of wild-type and K232M mutant AtIPMDH2 crystal structures.** The AtIPMDH2·IPM·Mg^{2+} complex (monomer A in *white*; monomer B in *gray*) and the K232M mutant (monomer A in *gold*; monomer B in *rose*) were overlaid, and key active site residues are displayed as *stick* renderings.

TABLE 2

Steady-state kinetic parameters

Average values ± S.E. (n = 3–5) are shown. Assays were performed as described with a fixed concentration of NAD^+ (1 mM) and varied concentrations of IPM (up to 10 mM depending on the K_m value). —, activity not detected.

	k_{cat}	K_m^{IPM}	k_{cat}/K_m^{IPM}
	min^{-1}	μM	$M^{-1}\ s^{-1}$
Wild type	274 ± 9	3.5 ± 0.6	1,303,000
L132A	28.0 ± 2.5	24.2 ± 6.9	19,290
L133A	186 ± 16	125 ± 25	24,830
R136A	—	—	—
R136K	2.0 ± 0.2	3,730 ± 530	9
R146A	1.8 ± 0.1	70.7 ± 4.1	429
R146K	1.4 ± 0.1	119 ± 27	192
R174A	—	—	—
R174K	97 ± 3	753 ± 62	2,140
Y181A	1.0 ± 0.1	8.3 ± 2.6	1,920
Y181F	14 ± 1	7.4 ± 1.7	32,320
Y181H	35 ± 3	6.3 ± 2.8	91,210
K232M	—	—	—
N234A	—	—	—
N234D	—	—	—
V235A	120 ± 38	11.4 ± 1.4	180,300
D264N	—	—	—
D288N	—	—	—
D292N	0.2 ± 0.1	27.8 ± 6.6	109

Arg-174 resulted in a loss of detectable activity, the R146A mutant retained activity with a 6,800-fold reduction in k_{cat}/K_m values (Table 2). Similarly, the R136K, R146K, and R174K mutations drastically compromised catalytic efficiency with 610–145,000-fold reductions (Table 2). Mutation of Arg-136 and Arg-146 altered both k_{cat} and K_m values for IPM. This suggests important roles for these residues in substrate binding and transition state stabilization during catalysis. The R174K mutant exhibited 3-fold lower turnover rates and 50-fold higher K_m values compared with wild type.

Site-directed mutagenesis of residues in the metal-binding site and residues that could function in general acid/base catalysis differentially alter the activity of AtIPMDH2. The aspartic acids that form the Mg^{2+}-binding site are extremely sensitive to changes in their carboxylate side chains, as the D264N and D288N mutants abrogated activity and the D292N mutation reduced k_{cat} by 1,500-fold (Table 2). Consistent with a possible role in acid/base catalysis, the K232M mutant was inactive but so was the N234A mutant. Substitution of Tyr-181, which has previously been proposed to be involved in acid/base chemistry (25), yielded modest 2–3-fold changes in K_m values with varied effects on turnover rates. The Y181A mutation lowered k_{cat} values nearly 400-fold with the Y181F and Y181H mutants displaying 19- and 8-fold reductions in turnover rate, respectively (Table 2).

Crystal Structure and ITC Analysis of the AtIPMDH2 K232M Mutant—The potential role of Lys-232 in the reaction mechanism and the loss of activity with the K232M mutant led us to examine the three-dimensional structure of this mutant. The x-ray structure of the AtIPMDH2 K232M mutant was determined at 1.83 Å resolution by molecular replacement (Table 1). The overall structure of the K232M mutant was similar to the AtIPMDH2 apoenzyme structure with a 0.8-Å r.m.s.d. for 358 C_α atoms. Comparison of the wild-type and K232M mutant structures shows that the active site in each enzyme is structurally similar, but with one major difference (Fig. 6). The positions of the arginine residues that interact with IPM are shifted slightly away from the active site in the mutant structure, which was crystallized without ligands and likely reflects the closure of the active site in the ligand-bound form. The most striking difference is the position of the methionine side chain in the K232M mutant compared with the lysine side chain of the wild-type enzyme. Instead of orienting toward the IPM-binding site, the methionine side chain of the K232M mutant points into an apolar patch defined by Phe-286 of monomer A and Ile-285 and Ile-289 of monomer B with a resulting 3.5-Å shift between the N_ζ of Lys-232 and C_ϵ of Met-232. This change in the K232M mutant creates space for Tyr-181 to tilt ~50° and adjusts 1.1 Å toward the space formerly occupied by Lys-232.

Given the loss of activity and the structural change in the active site of the K232M mutant, ITC was used to compare the binding of IPM and NAD^+ to the wild-type and mutant enzymes (Fig. 7; Table 3). Binding of IPM and NAD^+ was endothermic and exothermic, respectively, for either protein. Fitting of the ITC data to a single-site binding model yielded stoichiometries consistent with one-to-one binding. IPM binding was not observed in the absence of Mg^{2+}. Overall, the K_d values for binding of each substrate to either wild-type or mutant AtIPMDH2 were comparable. This indicates that the observed

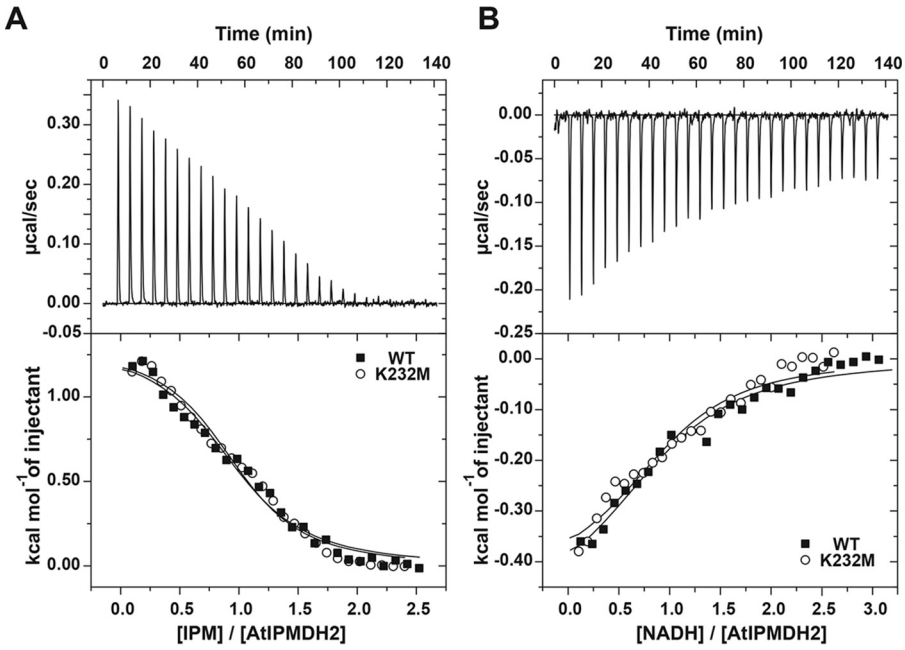

FIGURE 7. **ITC analysis of substrate binding to AtIPMDH2.** *A,* titration of IPM to wild type (*WT*; ■) and K232M mutant (○) AtIPMDH2. ITC data (*upper panel*) are plotted as heat signal *versus* time. In the *lower panel,* the integrated heat responses per injection are shown. *Solid lines* represent the fit to data using a single-site binding model. *B,* titration of NAD^+ to wild type (■) and K232M mutant (○) AtIPMDH2. ITC data (*upper panel*) are plotted as heat signal *versus* time. In the *lower panel*, the integrated heat responses per injection are shown. *Solid lines* represent the fit to data a single-site binding model.

TABLE 3

ITC analysis of ligand binding to wild-type and K232 M mutant AtIPMDH2

All titrations were performed as described under "Experimental Procedures." ITC data were fit to a single-site binding model with average values ± S.E. ($n = 3$) shown.

Protein-ligand	n	K_d	ΔG	ΔH	$-T\Delta S$
		μM	*kcal mol*$^{-1}$	*kcal mol*$^{-1}$	*kcal mol*$^{-1}$
Wild type-IPM	0.99 ± 0.03	8.3 ± 1.7	−6.71 ± 1.39	1.30 ± 0.06	−8.01
K232M-IPM	1.00 ± 0.03	7.4 ± 1.5	−7.26 ± 1.34	1.29 ± 0.05	−8.04
Wild type-NADH	0.95 ± 0.08	19.3 ± 4.7	−6.21 ± 1.52	−0.50 ± 0.05	−5.70
K232M-NADH	0.98 ± 0.07	17.9 ± 5.4	−6.26 ± 1.87	−0.44 ± 0.05	−5.82

structural difference in the K232M mutant does not alter protein-substrate interaction.

Discussion

The evolution of specialized metabolic pathways in plants and microbes involves proteins that retain common chemical mechanisms but with diversified substrate specificities. The adaptation of IPMDH from leucine biosynthesis into a 3-(2′-methylthio)ethylmalate dehydrogenase for production of aliphatic glucosinolates is one of many such examples (9, 10). The overall conservation of active site residues in the IPMDH and 3-(2′-methylthio)ethylmalate dehydrogenase (*i.e.* AtIPMDH1) from Arabidopsis allows for structure/function studies of AtIPMDH2 to provide insight on the oxidative decarboxylation step of both leucine- and methionine-derived glucosinolate synthesis in plants.

Structurally, AtIPMDH2 shares a common three-dimensional fold (Fig. 2) with other β-hydroxyacid oxidative decarboxylases, including bacterial IPMDH (50–60% sequence identity), bacterial homoisocitrate dehydrogenases (~40% sequence identity), and bacterial and yeast isocitrate dehydrogenases (25–30% sequence identity) (25). As suggested by sequence comparisons of residues in the NAD(H)-binding sites of AtIPMDH2 and structurally related proteins (Fig. 3*C*), the requirement for binding nicotinamide cofactors appears to be a major constraint on the overall fold of the β-hydroxyacid oxidative decarboxylase enzyme family. Although the IPMDH from various organisms use NAD(H) as a cofactor, some forms of isocitrate dehydrogenase prefer NADP(H) and contain additional substitutions (*i.e.* lysine and arginine residues) that allow for specific interaction with the 2′-phosphate group (20).

Comparison of the apoenzyme and NAD^+-bound forms of AtIPMDH2 indicate that conformational changes are required for bringing residues on opposite sides of the extended cleft into proximity of NAD(H) (Fig. 3). The movement of the exterior side of the AtIPMDH2 monomer (Fig. 3*D*) toward the dimer interface positions the β1i-α9 loop (*i.e.* residues 320–340) as a clamp over the bound cofactor (Fig. 3, *B* and *D*). Small-angle x-ray scattering studies and subsequent crystal structures of the bacterial IPMDH show similar conformational changes (20, 22, 26). Although the steady-state kinetic mechanism of IPMDH is unclear, ITC analysis (Fig. 7; Table 3) indicates that either substrate can bind to free enzyme. However, the location of the IPM and Mg^{2+}-binding sites deeper in the active site cleft (Fig. 4) (*i.e.* behind NAD(H)) suggests that an ordered addition is preferred for formation of a catalytic complex.

The structure of the AtIPMDH2·IPM·Mg^{2+} complex provides a detailed view of interactions and a plausible molecular basis for the evolution of 3-(2′-methylthio)ethylmalate dehy-

drogenase activity in AtIPMDH1 (Fig. 4). Previous studies identified the point mutation of Leu-133 in AtIPMDH2 to a phenylalanine in AtIPMDH1 as critical for the evolution of 3-(2′-methylthio)ethylmalate dehydrogenase activity (9). In the x-ray crystal structure, the γ-isopropyl group of IPM is toward Leu-133. For aliphatic glucosinolate production, the γ-isopropyl group is replaced with a 2-methylthioethyl substituent, which requires additional space for binding. Because a phenylalanine substitution at position 133 introduces a larger side chain at this position, presumably there is a structural change that allows for steric accommodation of the glucosinolate biosynthesis substrate. Moreover, because subsequent reactions during methionine-derived glucosinolate production extend the aliphatic group from C2 to C8 (9, 10), these longer molecules also fit within the AtIPMDH1 active site. The localized differences in the substrate site of AtIPMDH1 remain to be determined.

Until recently, only limited functional analysis of IPMDH from either plant or bacterial sources with regard to catalysis has been described. Site-directed mutagenesis of the tyrosine corresponding to Tyr-181 to a phenylalanine in the IPMDH from *T. thermophilus* resulted in a greater than 10-fold reduction in specific activity (27). Other mutational studies of the *T. thermophilus* IPMDH (28), which is also K^+-dependent unlike the plant enzyme, targeting the lysine-tyrosine pair and aspartate residues, complement the structure-function analysis presented here. Interestingly, comparative analysis of members of the β-hydroxyacid oxidative decarboxylases suggests that the lysine-tyrosine pair is critical for catalysis (25); however, conflicting proposals for the roles of these residues in the enzyme family have been made.

Steady-state kinetic analysis of point mutants in residues (Leu-132, Leu-133, and Val-235) surrounding the γ-isopropyl group of IPM (Fig. 4*A*) revealed less dramatic changes in k_{cat}/K_m values than substitutions in the arginine residues (Arg-136, Arg-146, and Arg-174; Fig. 4*A*) that interact with the substrate carboxylate groups (Table 2). In particular, the effects of the R136A and R136K mutants on AtIPMDH2 suggest that this arginine is a major driver of IPM interaction, as substitutions of Arg-136 displayed the largest reduction in catalytic efficiency compared with mutations of either Arg-146 or Arg-174. Overall, the cluster of arginines is important for IPM binding and contributes to transition state stabilization during the oxidative decarboxylation of IPM to 4-methyl-2-oxovalerate. As observed in multiple β-hydroxyacid oxidative decarboxylases (25), the aspartates that coordinate the Mg^{2+} ion and substrate in AtIPMDH2 were highly sensitive to changes in the side chain (Table 2), as the D264N and D288N mutants displayed no detectable activity and the D292N mutant was severely impaired. In addition, the short (2.3 Å) distances between the Mg^{2+} ion and the side chains of Asp-264, Asp-288, and Asp-292, and the α-carboxylate of IPM reinforce the critical role of charge-charge interactions in the active site. The structures and biochemical analysis of residues in the AtIPMDH2 active site indicate that multiple residues are key for interaction with IPM, but what are the roles of Lys-232, Tyr-181, and Asn-234 in the AtIPMDH2 active site?

Early structural studies of the bacterial IPMDH led to a proposed mechanism based entirely on three-dimensional comparisons with isocitrate dehydrogenase (20–22), in which the lysine-tyrosine pair is central to the oxidative decarboxylation reaction. In these mechanisms, the lysine was proposed to act as a general base with the tyrosine abstracting a proton to initiate catalysis (25, 29). In other β-hydroxyacid oxidative decarboxylases, such as 6-phosphoglucoonate dehydrogenase, a proximal glutamate has also been proposed to serve a similar role as the tyrosine (30). Now, a combination of x-ray structures and biochemical data allows for a refinement to the reaction mechanism of IPMDH.

Examination of the AtIPMDH2 active site with IPM bound (Fig. 5) shows that 3.7 Å separates the N_ζ of Lys-232 and the hydroxyl group of Tyr-181, which makes it unlikely that the tyrosine deprotonates the amine for catalysis. Moreover, the AtIPMDH2 Y181A, Y181F, and Y181H mutants do not show reductions in k_{cat} that would be expected for the loss of a general acid/base required for activation of the lysine (Table 2). The catalytic lysine has also been suggested to act as a general base that abstracts a proton from the hydroxyl group of IPM; however, the amine of the Lys-232 is 3.4 Å away from substrate. Inspection of the active site shows a water molecule bound by Lys-232 (2.9 Å), Asn-234 (3.1 Å), and Asp-264 (2.8 Å) that is also positioned 3.2 Å from the hydroxyl group of IPM. This suggests an alternate mechanism that still centers on Lys-232 but also involves this water molecule (Fig. 8).

In the proposed reaction mechanism for IPMDH (Fig. 8), Lys-232 abstracts a proton from the water molecule, which in turn functions as a general base to accept a proton from the substrate hydroxyl group with transfer of a hydride to NAD^+. Superimposition of the AtIPMDH2 structures (Fig. 5) indicates that the C4-position of the cofactor is 3.0 Å from the substrate. Recent pK_a calculations and quantum mechanical/molecular mechanics simulations suggest that the protonation state of the lysine in the *T. thermophilus* IPMDH active site depends on local environment and favors an unprotonated amine in the resting state (28). The key role for Lys-232 in the reaction mechanism is supported by enzyme assays indicating a loss of activity for the K232M mutant, the x-ray crystal structure of the K232M mutant that shows structural changes in the active site largely limited to the introduced residue (Fig. 6), and ITC analysis demonstrating unchanged binding of either IPM or NAD^+ (Fig. 7; Table 3). This suggestion is also consistent with pH effects associated with mutation of the catalytic lysine in the *T. thermophilus* IPMDH and with quantum mechanical/molecular mechanics simulations suggesting a similar mechanism involving an active site water molecule (28). Moreover, the loss of activity observed in the AtIPMDH2 N234A mutant may result from altered positioning of the water molecule. Next, the Mg^{2+} ion, serving as a Lewis acid, facilitates decarboxylation of the β-keto acid with the active site water molecule functioning as a general acid. The resulting enol undergoes tautomerization to the ketone product. It is not clear whether this occurs in solution following release of products or within the enzyme active site. In the bacterial IPMDH and isocitrate dehydrogenase, unusual pH profiles for enzymes with point mutations in the tyrosine have been interpreted as evidence for this residue serving as a general acid in the protonation of the enolate intermediate after decarboxylation (25, 28).

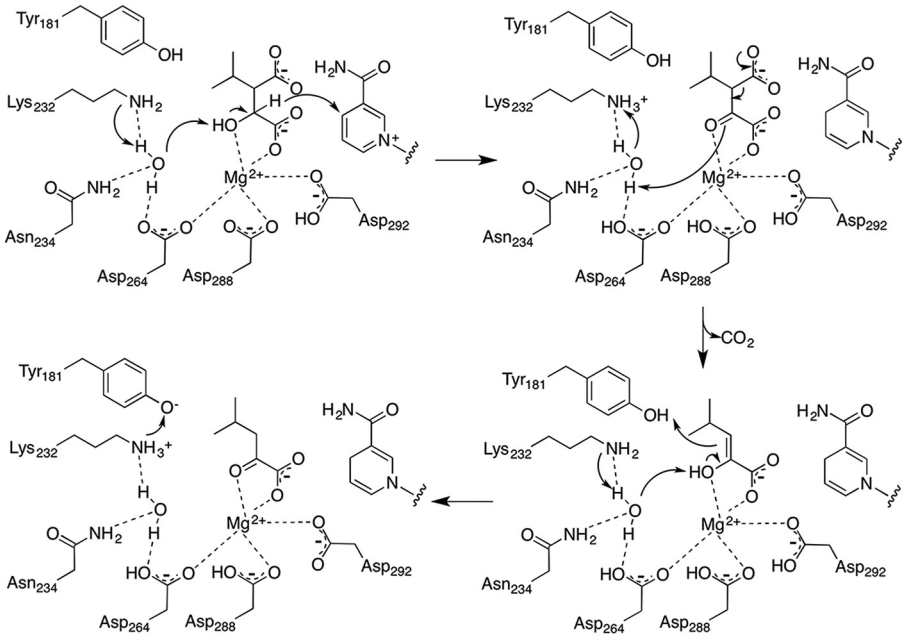

FIGURE 8. **Proposed reaction mechanism of IPMDH.**

Overall, IPMDH and other enzymes of the β-hydroxyacid oxidative decarboxylase family are examples of how different active site features (*i.e.* a water molecule in IPMDH *versus* a tyrosine in isocitrate and homoisocitrate dehydrogenases) can be used for similar chemical purposes and how subtle variations in the IPMDH active site can contribute to specialized metabolism. Retention of the same chemical reaction in the IPMDH homologs from leucine biosynthesis and aliphatic glucosinolate biosynthesis pathways are great examples of this evolutionary process.

Author Contributions—S. G. L. and J. M. J. designed the research; S. G. L. and R. N. performed the research; S. G. L, R. N., and J. M. J. analyzed the data and wrote and edited the manuscript.

References

1. Ober, D. (2005) Seeing double: gene duplication and diversification in plant secondary metabolism. *Trends Plant Sci.* **10,** 444–449
2. Halkier, B. A., and Gershenzon, J. (2006) Biology and biochemistry of glucosinolates. *Annu. Rev. Plant Biol.* **57,** 303–333
3. Kroymann, J. (2011) Natural diversity and adaptation in plant secondary metabolism. *Curr. Opin. Plant Biol.* **14,** 246–251
4. Agerbirk, N., and Olsen, C. E. (2012) Glucosinolate structures in evolution. *Phytochemistry* **77,** 16–45
5. Schuster, J., Knill, T., Reichelt, M., Gershenzon, J., and Binder, S. (2006) Branched-chain aminotransferase4 is part of the chain elongation pathway in the biosynthesis of methionine-derived glucosinolates in Arabidopsis. *Plant Cell* **18,** 2664–2679
6. Knill, T., Schuster, J., Reichelt, M., Gershenzon, J., and Binder, S. (2008) *Arabidopsis* branched-chain aminotransferase 3 functions in both amino acid and glucosinolate biosynthesis. *Plant Physiol.* **146,** 1028–1039
7. Textor, S., Bartram, S., Kroymann, J., Falk, K. L., Hick, A., Pickett, J. A., and Gershenzon, J. (2004) Biosynthesis of methionine-derived glucosinolates in *Arabidopsis thaliana*: recombinant expression and characterization of methylthioalkylmalate synthase, the condensing enzyme of the chain-elongation cycle. *Planta* **218,** 1026–1035
8. Textor, S., de Kraker, J. W., Hause, B., Gershenzon, J., and Tokuhisa, J. G. (2007) MAM3 catalyzes the formation of all aliphatic glucosinolate chain lengths in *Arabidopsis*. *Plant Physiol.* **144,** 60–71
9. He, Y., Mawhinney, T. P., Preuss, M. L., Schroeder, A. C., Chen, B., Abraham, L., Jez, J. M., and Chen, S. (2009) A redox-active isopropylmalate dehydrogenase functions in the biosynthesis of glucosinolates and leucine in *Arabidopsis*. *Plant J.* **60,** 679–690
10. He, Y., Galant, A., Pang, Q., Strul, J. M., Balogun, S. F., Jez, J. M., and Chen, S. (2011) Structural and functional evolution of isopropylmalate dehydrogenases in the leucine and glucosinolate pathways of *Arabidopsis thaliana*. *J. Biol. Chem.* **286,** 28794–28801
11. Ellerström, M., Josefsson, L. G., Rask, L., and Ronne, H. (1992) Cloning of a cDNA for rape chloroplast 3-isopropylmalate dehydrogenase by genetic complementation in yeast. *Plant Mol. Biol.* **18,** 557–566
12. Jackson, S. D., Sonnewald, U., and Willmitzer, L. (1993) Cloning and expression analysis of β-isopropylmalate dehydrogenase from potato. *Mol. Gen. Genet.* **236,** 309–314
13. Nozawa, A., Takano, J., Miwa, K., Nakagawa, Y., and Fujiwara, T. (2005) Cloning of cDNAs encoding isopropylmalate dehydrogenase from *Arabidopsis thaliana* and accumulation patterns of their transcripts. *Biosci. Biotechnol. Biochem.* **69,** 806–810
14. He, Y., Chen, L., Zhou, Y., Mawhinney, T. P., Chen, B., Kang, B. H., Hauser, B. A., and Chen, S. (2011) Functional characterization of *Arabidopsis thaliana* isopropylmalate dehydrogenases reveals their important roles in gametophyte development. *New Phytol.* **189,** 160–175
15. Otwinowski, Z., and Minor, W. (1997) Processing of x-ray diffraction data collected in oscillation mode. *Methods Enzymol.* **276,** 307–326
16. McCoy, A. J., Grosse-Kunstleve, R. W., Adams, P. D., Winn, M. D., Storoni, L. C., and Read, R. J. (2007) Phaser crystallographic software. *J. Appl. Crystallogr.* **40,** 658–674
17. Emsley, P., Lohkamp, B., Scott, W. G., and Cowtan, K. (2010) Features and developmen of Coot. *Acta Crystallogr. D Biol. Crystallogr.* **66,** 486–501
18. Adams, P. D., Afonine, P. V., Bunkóczi, G., Chen, V. B., Davis, I. W., Echols, N., Headd, J. J., Hung, L. W., Kapral, G. J., Grosse-Kunstleve, R. W., McCoy, A. J., Moriarty, N. W., Oeffner, R., Read, R. J., Richardson, D. C., *et al.* (2010) PHENIX: a comprehensive Python-based system for macromolecular structure solution. *Acta Crystallogr. D Biol. Crystallogr.* **66,** 213–221
19. Imada, K., Sato, M., Tanaka, N., Katsube, Y., Matsuura, Y., and Oshima, T. (1991) Three-dimensional structure of a highly thermostable enzyme, 3-isopropylmalate dehydrogenase of *Thermus thermophilus* at 2.2 A resolution. *J. Mol. Biol.* **222,** 725–738
20. Hurley, J. H., and Dean, A. M. (1994) Structure of 3-isopropylmalate dehydrogenase in complex with NAD^+: ligand-induced loop closing and

mechanism for cofactor specificity. *Structure* **2,** 1007–1016
21. Imada, K., Inagaki, K., Matsunami, H., Kawaguchi, H., Tanaka, H., Tanaka, N., and Namba, K. (1998) Structure of 3-isopropylmalate dehydrogenase in complex with 3-isopropylmalate at 2.0 A resolution: the role of Glu88 in the unique substrate-recognition mechanism. *Structure* **6,** 971–982
22. Wallon, G., Kryger, G., Lovett, S. T., Oshima, T., Ringe, D., and Petsko, G. A. (1997) Crystal structures of *Escherichia coli* and *Salmonella typhimurium* 3-isopropylmalate dehydrogenase and comparison with their thermophilic counterpart from *Thermus thermophilus*. *J. Mol. Biol.* **266,** 1016–1031
23. Miyazaki, J., Asada, K., Fushinobu, S., Kuzuyama, T., and Nishiyama, M. (2005) Crystal structure of tetrameric homoisocitrate dehydrogenase from an extreme thermophile, *Thermus thermophilus*: involvement of hydrophobic dimer-dimer interaction in extremely high thermotolerance. *J. Bacteriol.* **187,** 6779–6788
24. Taylor, A. B., Hu, G., Hart, P. J., and McAlister-Henn, L. (2008) Yeast isocitrate dehydrogenase with citrate bound in the regulatory subunits. *J. Biol. Chem.* **283,** 10872–10880
25. Aktas, D. F., and Cook, P. F. (2009) A lysine-tyrosine pair carries out acid-base chemistry in the metal ion-dependent pyridine dinucleotide-linked β-hydroxyacid oxidative decarboxylases. *Biochemistry* **48,** 3565–3577
26. Kadono, S., Sakurai, M., Moriyama, H., Sato, M., Hayashi, Y., Oshima, T., and Tanaka, N. (1995) Ligand-induced changes in the conformation of 3-isopropylmalate dehydrogenase from *Thermus thermophilus*. *J. Biochem.* **118,** 745–752
27. Miyazaki, K., and Oshima, T. (1993) Tyr-139 in *Thermus thermophilus* 3-isopropylmalate dehydrogenase is involved in catalytic function. *FEBS Lett.* **332,** 37–38
28. Gráczer, É., Szimler, T., Garamszegi, A., Konarev, P. V., Lábas, A., Oláh, J., Palló, A., Svergun, D. I., Merli, A., Závodszky, P., Weiss, M. S., and Vas, M. (2016) Dual role of the active site residues of *Thermus thermophilus* 3-isopropylmalate dehydrogenase: chemical catalysis and domain closure. *Biochemistry* **55,** 560–574
29. Karsten, W. E., Liu, D., Rao, G. S., Harris, B. G., and Cook, P. F. (2005) A catalytic triad is responsible for acid-base chemistry in the *Ascaris suum* NAD-malic enzyme. *Biochemistry* **44,** 3626–3635
30. Karsten, W. E., Chooback, L., and Cook, P. F. (1998) Glutamate 190 is a general acid catalyst in the 6-phosphogluconate-dehydrogenase-catalyzed reaction. *Biochemistry* **37,** 15691–15697

Structure and Mechanism of Isopropylmalate Dehydrogenase from *Arabidopsis thaliana* : INSIGHTS ON LEUCINE AND ALIPHATIC GLUCOSINOLATE BIOSYNTHESIS

Soon Goo Lee, Ronald Nwumeh and Joseph M. Jez

J. Biol. Chem. 2016, 291:13421-13430.
doi: 10.1074/jbc.M116.730358 originally published online May 2, 2016